# Neutrino Telescope Array Letter of Intent:

A Large Array of High Resolution Imaging Atmospheric Cherenkov and Fluorescence Detectors for Survey of Air-showers from Cosmic Tau Neutrinos in the PeV-EeV Energy Range

Makoto Sasaki\*1 and George Wei-Shu Hou<sup>†2</sup>

<sup>1</sup>ICRR, The University of Tokyo, Kashiwa, Chiba 277-8582, Japan <sup>2</sup>Department of Physics, National Taiwan University, Taipei 10617, Taiwan

July 20, 2015

#### Abstract

This Letter of Intent (LoI) describes the outline and plan for the Neutrino Telescope Array (NTA) project. High-energy neutrinos provide unique and indisputable evidence for hadronic acceleration, as well as a most accurate probe into the hidden sector of traditional astronomy or physics, such as dark matter. However, their extremely low flux and interaction cross section make their detection extraordinarily difficult. Recently, IceCube has reported astronomical neutrino candidates in excess of expectation from atmospheric secondaries, but is limited by the water Cherenkov detection method. A next generation high-energy neutrino telescope should be capable of establishing indisputable evidence for cosmic high-energy neutrinos. It should not only have orders-of-magnitude larger sensitivity, but also enough pointing accuracy to probe known or unknown astronomical objects, without suffering from atmospheric secondaries. The proposed installation is a large array of compound eye stations of imaging atmospheric Cherenkov and fluorescence detectors, with wide field of view and refined observational ability of air showers from cosmic tau neutrinos in the PeV-EeV energy range. This advanced optical complex system is based substantially on the development of All-sky Survey High Resolution Air-shower detector (Ashra) and applies the tau shower Earth-skimming method to survey PeV-EeV  $\nu_{\tau}$ s. It allows wide (30°×360°) and deep (~400 Mpc) survey observation for PeV-EeV  $\nu_{\tau}$ s assuming the standard GRB neutrino fluence. In addition, it enjoys the pointing accuracy of better than  $0.2^{\circ}$  in essentially background-free conditions. With the advanced imaging of Earth-skimming tau showers in the wide field of view, we aim for clear discovery and identification of astronomical  $\nu_{\tau}$  sources, providing inescapable evidence of the astrophysical hadronic model for acceleration and/or propagation of extremely high energy protons in the precisely determined direction. In this LoI, we present main features of the NTA detector, scientific goal and observational objects, Earth-skimming detection method, the NTA detector, the expected detector performance, and brief summaries of time frame, organization, and funding.

**Keywards:** Astroparticle physics, Neutrino astronomy, Hadron acceleration, Cosmic ray origin, Dark matter, Gamma ray burst, Active galactic nuclei, Neutrino telescope, PeV-EeV neutrinos, Earth-skimming detection, Tau neutrino, Ashra, Neutrino Telescope Array

<sup>\*</sup>sasakim@icrr.u-tokyo.ac.jp

<sup>†</sup>wshou@phys.ntu.edu.tw

### 1 Introduction

### 1.1 Background and Past-related Achievements

High-energy neutrinos uniquely provide indisputable evidence for hadronic acceleration in the universe. High-energy charged cosmic rays have been observed for a long time, but their origin is still a mystery. The energy spectrum follows globally a broken  $E^{-\alpha}$  power law, where  $\alpha=2.7\sim3.1$ , which indicates shock acceleration. Several astronomical object classes have been proposed as potential hadronic accelerators. The galactic and extragalactic magnetic fields prevent us from using the arrival direction observed on Earth to reveal the actual sources. So far, standard astronomical observational data, spanning the electromagnetic wavelengths from radio to  $\gamma$ -ray, have not succeeded in revealing direct evidence of the non-thermal process. On the other hand, high-energy neutrinos should be produced at the accelerators through charged pion production in collisions with radiation fields or the ambient matter, in reactions such as:

$$p + \gamma \to \Delta^+ \to \pi^0 + p, \ \pi^+ + n$$
  
 $p + \text{nucleus} \to \pi + X \ (\pi = \pi^0, \pi^{\pm})$ .

Subsequent decay gives the approximate neutrino flavour ratio  $\nu_e:\nu_\mu:\nu_\tau=1:2:0$  at the sources, which is turned into the ratio of  $\nu_e:\nu_\mu:\nu_\tau=1:1:1$  by neutrino oscillation upon arrival at Earth. The photopion  $(p\gamma)$  reaction is typically the main neutrino generation process where extra galactic sources like jets and cores of active galactic nuclei (AGN) and  $\gamma$ -ray burst (GRB) jets have been widely studied. Some sources like starburst galaxies (SBGs) may emit the neutrino fluxes mainly through the hadronuclear (pp) reaction [1]. For many astronomical objects, ambient photons are expected to be in the UV region. In that case, the kinetic threshold for photopion production through delta resonance is in the range of several PeV.

The IceCube Collaboration claims the first observation of two PeV-Energy neutrinos, with moderate 2.8  $\sigma$  excess over Monte Carlo expectation of background events [2]. They further extended their analysis to lower energy region [3]. Fitting to the observed photoelectron spectrum, they estimate the diffuse neutrino flux to be  $E^2\phi_{\nu_e+\nu_\mu+\nu_\tau}=3.6\times 10^{-8}$  GeV sr<sup>-1</sup> s<sup>-1</sup>, assuming an  $E^{-2}$  power law flux. The fact that no more events occur in the higher energy region favours neutrinos from astronomical objects but not cosmogenic neutrinos [4], if the events are true neutrino signals. Assuming astronomical objects where the observed neutrinos were produced, the estimated fluences of the neutrino beams are rather high. It therefore becomes plausible that a next generation high-energy neutrino telescope, with higher sensitivity for high-energy neutrinos and wide field of view, could make clear discovery of hadron accelerators in the Universe.

For cosmogenic neutrinos, produced by the photopion process of protons with the cosmic microwave background, the energy threshold is around  $10^{19.6}$  eV. However, the Pierre Auger Observatory (Auger) claims that heavier components dominate the highest energy region around  $10^{19.6}$  eV [5]. If true, the flux estimate of cosmogenic neutrinos is much suppressed. Both the cosmic ray flux spectrum around threshold and the density of cosmic microwave background are observed so well, the detection of cosmogenic neutrinos provide a good check of the Auger results on cosmic ray composition. Besides high-energy neutrino detection, the observation of PeV  $\gamma$ -rays could also have provided a clear proof of hadron acceleration, from the subsequent  $\pi^0 \to \gamma \gamma$  decay in the above process. However, in the PeV range, photons are absorbed by interaction with cosmic microwave photons into electron pairs. Therefore, especially the observation of PeV-EeV neutrinos with precise pointing accuracy would provide unique and particularly important identification of astronomical cosmic ray

origins, as well as examination of cosmogenic neutrino production from extragalactic hadron propagation.

A final answer to the mystery of cosmic ray origins requires the observation of high-energy neutrinos. High-energy neutrinos can be the most accurate probe into hidden sector of traditional astronomy or physics, such as dark matter. However, their extremely low flux and interaction cross section make their detection extraordinarily difficult. To discover clear, indisputable evidence of cosmic high-energy neutrinos, a next generation detector should have orders-of-magnitude larger sensitivity. To probe into the association with known or unknown astronomical objects as a telescope for very high-energy (VHE) neutrinos with the energies above 1 PeV, it should also have enough pointing accuracy, without suffering from background events of atmospheric secondaries.

The Earth-skimming tau neutrino technique enjoys a large target mass by detecting extensive air-showers produced by tau lepton decays in the atmosphere. The tau leptons, produced by VHE tau neutrinos that interact with the Earth matter they traverse, emerge out of a mountain or the ground facing the detector. This method has detection sensitivity in the PeV-EeV region, and can be used to search for neutrinos originating from hadron acceleration in astronomical objects. Additional advantages are perfect shielding of cosmic ray secondaries, precise arrival direction determination, and negligible background from atmospheric neutrinos.

The All-sky Survey High Resolution Air-shower detector Phase I (Ashra-1) is an optical-telescope based detector system [6] optimized to detect VHE particles aiming for "multi-particle astronomy" [7, 8]. It is distinguished by two features: (1) an ultra wide optical system in which 42-degree FOV (field of view) is demagnified to 1-inch diameter phospher screen on an output window by using photon and electron optics [9]; (2) high resolution imaging system with a trigger. Ashra-1 combines these unique features, resulting in very cost-effective pixels compared to conventional photomultiplier arrays at the focal surface of an optical telescope (Fig. 1). Ashra-1 can observe the whole sky with a few arc minutes resolution, with 12 detector units pointing at different directions, where a detector unit consists of a few Light Collectors (LC) pointing at the same direction.

The Ashra-1 detector system is designed so that the focal image is split into trigger/image capture devices after amplification. This feature enables one to simultaneously access 3 kinds of phenomena that have different time scales, i.e., Cherenkov emission (ns), fluorescence ( $\mu$ s), and starlight (s), without sacrificing the signal to noise ratio. By fully utilizing these distinct features, Ashra aims to undertake full-fledged astronomical observation using VHE particles, commencing with the first detection of VHE neutrinos using Earth and mountain as target [10]. It can also be used to optically observe transient objects like GRBs, as it monitors the whole sky simultaneously [11, 12]. The principal demonstration phase, Ashra-1, has been running at the Mauna Loa site at 3300 m above sea level on Hawaii Island since 2008. The deployed main and sub stations at the Mauna Loa site are shown in Fig. 2 Ashra-1 succeeded in the first search for PeV-EeV tau neutrinos originating from a GRB in the commissioning run [10], demonstrating the great sensitivity around 100 PeV with the earth-skimming  $\nu_{\tau}$  technique. Ashra-1 has achieved the best instantaneous sensitivity in the energy region around 100 PeV since January 2012 after trigger upgrade.

The NuTel [13] project, conceived and started in 2001, was an effort concurrent with the development of Ashra-1. It purposed the fast construction of a limited neutrino telescope for detecting  $\nu_{\tau}$ -originated air-showers in the energy range of 1 to 1000 PeV, with possible sources such as AGNs, GRBs, the Galactic Center (GC), etc. It took in the possibility of a base up the smaller Mt. Hualalai, which provides a wide baseline view of Mauna Loa. A multi-anode PMT-based readout electronics, aimed for Cherenkov light in the UV, was quickly built, but the project got cut since 2004. The group still built two 2m telescopes,





Figure 1: An Ashra-1 light collector toward Mauna Kea.

Figure 2: The Ashra-1 main and sub stations at the Mauna Loa site.

and conducted a mountain test up 2200 m in Taiwan. An issue was the estimated event rate of  $\sim 0.5$  events per year, which was not quite convincing. This is where the well developed Ashra-1 comes in contrast: a mature VHE neutrino telescope, which we will call NTA, is at hand.

#### 1.2 Main Features of the NTA Detector

The key technical feature of the Ashra-1 detector rests on the use of electrostatic lenses, rather than optical lens systems, to generate convergent beams. This enables us to realise a high resolution over a wide field of view. This electron optics requires:

- wide angle high precision optics [14]; a Schmidt type optical system with modified Baker-Nunn optics allows a compromise between wide 42° field of view and 1 arc min resolution on the focal sphere of the light collector (Fig. 1), with pupil diameter of 1 m;
- photoelectric lens imaging-tube [9]; in addition to the optical system, the world's largest imaging-tube uses electrostatic lens to generate convergent beams from photo cathode of 20 inch diameter to output phosphorus window of 1 inch diameter, enabling a very low cost and high performance image sensor that provides high resolution over a wide FOV; and
- image pipeline [15]; the image transportation from imaging-tube (image intensifier) to a trigger device and image sensor of fine pixels (CCD+CMOS) with high gain and resolution, enables very fine images with parallel self-trigger systems that trigger for optical flash, atmospheric Cherenkov and fluorescence light separately.

Based on these achievements from Ashra-1, we start to form a new collaboration for realizing the next generation large Neutrino Telescope Array (NTA). The conceptual layout for the NTA observatory considers three site stations for a 25 km-side triangle, watching the total air mass surrounded by the mountains of Mauna Loa, Mauna Kea, and Hualalai (Fig. 3). A single site station at the center of the triangle has half-sky coverage. This configuration allows for tremendous instantaneous sensitivity (equivalent to >100 giga ton water), with Cherenkov-fluorescence stereoscopic observation for PeV-EeV neutrinos in essentially background-free conditions. With the demonstrated fine imaging of Earth-skimming tau showers and the significant improved detection solid angle (30° × 360°) for incoming tau neutrinos, we aim for clear discovery and identification of astronomical tau neutrino sources. Also interesting is the unique capability of cross observation between optical flashes, TeV-PeV  $\gamma$  rays, and PeV-EeV  $\nu_{\tau}$ s, once one or more of these three kinds of self-triggers are observed and associated with an astronomical object.



Figure 3: Layout of the NTA Observatory. Shaded region consists of three semicircles centered at Site1-3.

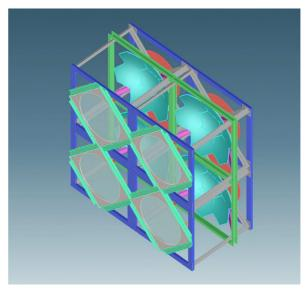


Figure 4: NTA detector unit of four light collectors of the same type.

From the current baseline design of the NTA detector system, each site has a group of detector units (DUs) for individual FOVs (Fig. 4). Each DU is composed of four LCs responsible for the same FOV. The LC has the design similar with Ashra-1 but with dimensions scaled up by 1.5 to gather more light. Each LC is instrumented with a pupil lens, seven segmented mirrors, a set of photoelectric imaging tube and image pipeline with a CMOS sensor. The DU has a unified trigger system which determine if image light gathered from four LCs through fiber-optic bundle transmission systems has enough confidence. Detailed design studies for the NTA detector are currently underway.

### 1.3 Scientific Goal and Observational Objectives

The main scientific goal of the NTA project is:

the clear discovery and identification of non-thermal hadronic process in the Universe.

This has not been directly confirmed by any observation so far and can be achieved by observing PeV-EeV neutrino emission as direct evidence and sensitive probe for collective processes that accelerate particles to energies many orders of magnitude beyond thermal energies. Fig. 5 shows measured and expected neutrino fluxes, and sensitive energy region of NTA with the sensitive energy range of PeV-EeV.

The multimessenger connection among Cosmic Rays, photons and neutrinos of different particles is crucial for comprehensive and deeper understandings of the fundamental non-thermal astrophysical processes. Multimessenger is a theme to much of the recent literature e.g. [16] [17] [18]. The measured fluxes of extremely-high energy cosmic rays (EHECR) with energies above 10<sup>18</sup> eV (EeV) inspire an associated flux of PeV-EeV cosmic neutrinos, although the production mechanisms of EHECR are still unknown. PeV-EeV neutrinos are predicted as a result of the decay of charged pions generated in interactions of EHECRs within the source objects (astrophysical neutrinos) and in their propagation through background photon fields (cosmogenic neutrinos) [19]. Cosmic rays up to and even beyond the PeV ("knee") are of Galactic origin. Around EeV between 10<sup>17</sup> and 10<sup>18.5</sup> eV ("ankle"), at maximum, known Galactic source candidates are generically considered running out of

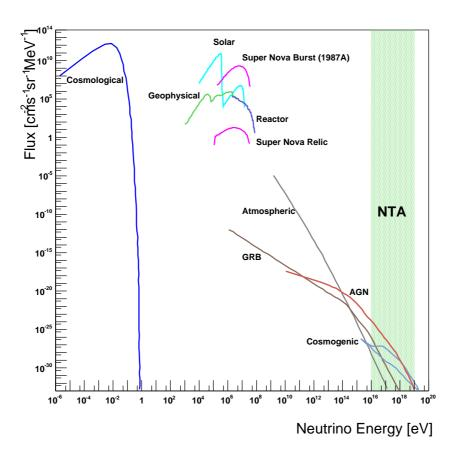


Figure 5: Measured and expected neutrino fluxes, and sensitive energy region of NTA (green band).

power and extragalactic sources start dominating the spectrum. On the other hand, from recent calculations, the maximum energy of accelerated particles may reach  $5 \times 10^{18}$  eV for Fe ions in Type IIb Supernova Remnants (SNRs) [20] [21]. Adding that, both the detailed composition and galactic-extragalactic transitions in the PeV-EeV region is still unclear and to be understood [22] [23] [24]. Simultaneous searches for PeV gamma rays and neutrinos would be useful to distinguish between galactic and extragalactic sources of cosmic rays [25]. If EHECRs are produced from Galactic point sources, then those point sources are also emitting PeV gamma rays. We note that the detection of galactocentric PeV gamma rays in the future would be a signature of the presence of EeV cosmic accelerators in the Milky Way [26]. EHECR sources in our galaxy will plausibly be investigated by the multimessenger approaches with very-high energy gamma rays and neutrinos in the PeV-EeV region, since the galactic size is within the observable distances of gamma rays around PeV even after the propagations in the background photons (Fig. 6).

IceCube recently reported the observation of three neutrinos with energies at 1-2 PeV [2] and 26 additional events at lower energies [3], which are significantly inconsistent with the background. Many authors have discussed the origins and physics scenarios of the IceCube signals in the context of multimessenger of EHECRs, VHE gammas, and VHE neutrinos among galactic and extragalactic sources, e.q. [17] [27].

The following potential candidates are considered as search objectives with the NTA survey.

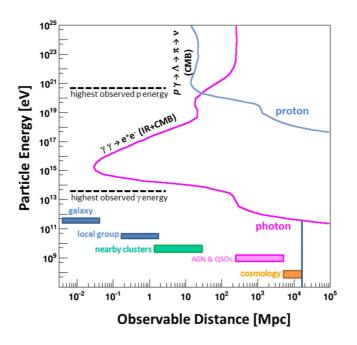


Figure 6: Particle energies and observable distances through the interactions with background photons with distance regions for sources (colored boxes), and the highest observed gamma and proton energies (dashed lines).

### • Galactic Sources:

The galactic supernova remnants (SNRs) are widely believed to be the dominant source for the cosmic rays (CRs) at energies below the knee around PeV, most probably through the diffusive shock acceleration mechanism [28]. Recent calculations show that Super Nova Remnant (SNR) acceleration in our galaxy can describe the whole energy spectrum of observed cosmic rays for the region from TeV up to the ankle, using different types of SNs and transition of composition in the galaxy [20]. Galactic GRBs, which are beamed away from Earth, can be the main source of Galactic cosmic rays at all energies [29]. From the observational point of view, Imaging Air Cherenkov Telescopes (IACTs) have detected more than hundreds of TeV  $\gamma$ -ray sources, including about 30 SNRs [30]. There are three classes of such objects: shell-type supernova remnants, pulsar wind nebulae, and binary systems. The expected neutrino fluxes from these sources and diffuse emission from cosmic ray interaction are calculated [31].

Shell-type Supernova remnants have long been considered as the likely acceleration site for the bulk of the galactic cosmic rays. The morphology of  $\gamma$ -ray emission from RXJ1713.7-3946 was studied [32]. A TeV  $\gamma$ -ray image of the SNR demonstrates that VHE particles are accelerated at the spatially resolved remnant, which has a shell morphology similar to that seen in X-rays. The energy spectrum indicates efficient acceleration of charged particles to energies beyond 100 TeV, consistent with current ideas of particle acceleration in young SNR shocks. Spatial correlations of the  $\gamma$ -ray emission with available target material seem to be present for the SNRs W28, IC443, RCW86 and RX J0852.0-4622 supernova in IACT data. The observations of  $\gamma$ -rays exceeding 10 TeV in the spectrum of the RX J0852.0-4622 supernova [33] has also strengthened the hypothesis that the hadronic acceleration is the process needed to explain the hard and intense TeV  $\gamma$ -ray spectrum. Such a correlation is also seen

in the region of the Galactic Centre (GC), where the acceleration site of the cosmic rays is not clear [34]. However, the directional distribution of the 21 cascade events suggests weakly significant excess ("hotspot") with a trial-corrected significance of 8 % [3]. Possible contributions from galactic neutrino sources like SNRs are consistent with the present diffuse  $\gamma$ -ray limits [35]. If the neutrino spectrum is dominated by galactic sources, the lack of observed CR anisotropy requires a soft neutrino spectrum with index  $\sim 2.3$  in the hadronuclear (pp) origin scenario [27]. The required index is consistent with a spectral index 2.2 of a point-like  $\gamma$ -ray source at the Galactic center, which was reported by H.E.S.S. [36]. The possibility of discrimination between pp and  $p\gamma$  source models by combining the measured neutrino and  $\gamma$ -ray fluxes, will be one example for the multimessenger approach [17].

Pulsar Wind Nebulae (PWNe) are some of the brightest TeV  $\gamma$ -ray sources. The central pulsar emits material into the nebulae such as the powerful Crab and Vela pulsars [37]. A significant fraction of nuclei is suggested to exist in pulsar winds [38]. The decay of pions produced in the interaction of these nuclei can dominate the TeV  $\gamma$ -ray emission, which suggests significant production of neutrinos should occur [39]. These nuclei and significant production of neutrinos may occur e.g. [39]. Pulsars could also be a strong source of very-high energy neutrinos [40], although there is a pessimistic estimate of the fluxes [41].

Binary systems of a compact object and a massive star are well established galactic TeV  $\gamma$ -ray sources, which are classified into binary PWN or microquasars. In the binary pulsar scenario, the spin-down of the neutron star is the energy source. In the microquasar scenario, accretion is the power-source, and particle acceleration occurs in relativistic jets produced close to the compact object (black hole or neutron star). The PSR 1259-63 system with 3.4-year period and the Be-star SS 2883 belong to the class of binary PWN. LS 5039 and LSI +61 303, are the remaining well established systems and expected as strong neutrino sources [42], of which acceleration site has not been revealed yet. Cyg X-1 is expected as the best  $\gamma$ -ray microquasar candidate, which hosts a black hole [43].

Undetected bright hard-spectrum sources beyond ~1 PeV could in principle be missed by current Cherenkov telescopes, since they have substantially reduced energy flux sensitivities in the higher energy region relative to their performance around 1 TeV. Due to the rapid rise of the effective detection area of NTA with energy, such sources could be promising candidates for the NTA detector. Several candidates for sources with hadron acceleration beyond 1 PeV have been identified in the Cygnus region by Milagro [44].

Our Galactic Center (GC) has also been proposed as neutrino sources. An intense diffuse emission of  $\gamma$ -rays with higher energies has been observed which likely implies the presence of a source of cosmic ray protons and thus of neutrinos [34]. The GC region is of particular interest because it is in the good sky view of NTA located on Hawaii Island in the northern hemisphere. A general scenario of Galactic  $\gtrsim 10$  PeV cosmic-ray interactions to produce PeV-EeV events [25], and plausible spectra of neutrino events as originating from Galactic cosmic rays [45], has been considered as well. IceCube has announced detection of 26 neutrino events with energies in the  $\sim 30$ -250 TeV range [3], in addition to the two events announced earlier with  $\sim 1$  PeV energy each [2]. The largest concentration of 5 shower-like events detected by IceCube is near the Galactic Center within uncertainties of their reconstructed directions. Adding that, IceCube observed 3 shower-like events which have their arrival directions consistent with the Fermi bubbles [46]. There is an absence of any track-like events in this region. Most of

the track-like events are out of the Galactic plane, and at least 4 of them are correlated with shower-like events in those regions [47].

#### • Extragalactic Sources:

As the extragalactic candidates for PeV-EeV neutrino emission, Gamma Ray Bursts (GRB), Active Galactic Nuclei (AGN) and galaxy clusters are well motivated. PeV-EeV neutrinos are also directly linked with the physics of proton acceleration to extremely high energy cosmic rays (EHECR) above EeV at cosmic ray origin objects. Recent measurements of the composition of EHECRs by the Pierre Auger Observatory (Auger) have suggested that the mean nuclear mass may increase with energy between 2 EeV and 35 EeV [5].

Gamma Ray Bursts (GRBs) eject the most energetic outflows in the observed Universe, with jets of material expanding relativistically into the surrounding interstellar matter with a Lorentz factor  $\Gamma$  of 100 or more. Energy dissipation processes involving nonthermal interactions between particles are thought to play an important role in GRBs, but remain observationally unresolved. The detection of PeV-EeV neutrinos  $(\nu s)$  from a GRB would provide direct evidence for the acceleration of hadrons into the EeV range, and of photopion interactions in the GRB. The GRB standard model [48], which is based on internal/external shock acceleration, has been used to describe the general features of a GRB and the observed multi-wavelength afterglow. However, the standard model cannot reproduce well the recent observational results [49]. The early X-ray afterglows detected by Swift exhibit a canonical behavior of steep-flat-steep in their light curve [50]. In some of GRBs, precursor activities were observed [51]. In some cases, the precursor preceded the main burst by several hundred seconds with significant energy emission. To better understand the ambiguous mechanisms of GRBs, observational probes of the optically thick region of the electromagnetic components, as well as hadron acceleration processes throughout the precursor, prompt, and afterglow phases are required. VHE  $\nu$ s can be used as direct observational probes, which are effective even in optically thick regions. The discovery of nearby low-luminosity (LL) GRB060218 suggests a much higher local event rate of LL-GRBs [52], which NTA can easily search for. NTA can check the ratio between the observed neutrino event rates from the Earth and the sky in the field of view of the detector, which means the measurement of the diffuse neutrino background from all GRBs with less systematic error.

Active Galactic Nuclei consist of super-massive black holes with  $10^6 \sim 10^9$  solar masses in their centre. The black hole radiates huge amount of energy typically of the order of  $10^{44}$  erg/s, which is transfered from gravitational energy after it accretes matter. The energy is expected to induce acceleration of particles. A special class of AGN, Blazers, has jet aligned closely to the line of sight, which can be strong gamma-ray sources. Many sources are reported at GeV and TeV energies by Fermi LAT [53]. Gamma ray emission from blazars is often highly variable, e.g. PKS 2155-304, with the most extreme variation observed an increase by two orders of magnitude within one hour [54]. We should observe the neutrino fluxes from such a source significantly within a short time. An observation of outburst from the blazar 1ES 1959+650 [55] suggests another type of neutrino sources, which is TeV emission without being accompanied by X-ray emission as synchrotron self-Compton (SSC) models typically predict. A hadronic model does not require TeV emission accompanied by X-ray emission. The observed flares are encouraging sites to search for high energy neutrino emission.

Starburst galaxies have unusually high rates of large-scale star formation processes. A

galactic-scale wind is driven by the collective effect of supernova explosions and massive stars at the central regions of the starburst galaxies. IACTs have detected the gamma ray flux at several hundred GeV from the starburst galaxies NGC253 and M82 [56] [57]. They suggests cosmic ray densities much higher than typical case expected in our own Galaxy by two to three orders of magnitude. The diffuse neutrino flux from all starburst galaxies is expected detectable with current detectors [1].

Cosmogenic Neutrinos are the secondary particles of the Greisen-Zatsepin-Kuzmin (GZK) process from the interaction of the highest energy cosmic rays with the cosmic microwave background [19, 58, 59]. Various cosmogenic neutrino models (for example [60]) which assume primary cosmic ray protons predict neutrino fluxes. They require  $4\pi$  solid angle averaged neutrino effective area  $A_{\nu}$  to be more than  $10^{-3}$  km<sup>2</sup> at 100 PeV to detect several cosmogenic neutrinos every year in case of full duty cycle. NTA satisfies this requirement well even assuming the duty of 10%.

The predicted flux has large uncertainties due to dependence on source spectrum and on spatial distribution and cosmological evolution of the sources [22]. If EHECRs are heavy nuclei like irons, the yield of the cosmogenic neutrino is strongly suppressed [61]. Therefore NTA has sufficient sensitivity for cosmogenic neutrinos to directly test the hypothesis of the observed highest energy cut-off of the cosmic ray spectrum due to a suppression induced by the GZK propagation of pure protons taking into account of the uncertainty of flux prediction even in the case of null result.

#### • Dark Matter and New Particles

Weakly Interacting Massive Particles (WIMPs) are favoured dark matter candidates, which are preferentially discussed in the minimal supersymmetric standard model (MSSM) framework [62]. Indirect WIMP detection use secondary particles such as  $\gamma_{\rm S}$ ,  $\nu_{\rm S}$ , weak bosons, tau pairs and so on from annihilations. Direct WIMP detection uses recoil nuclei from elastic WIMP-nucleus scattering. There is some complementarity between direct and indirect searches for dark matter, given the astrophysical assumptions inherent to the calculations. Both methods are sensitive to opposite extremes of the velocity distribution of dark matter particles in the Galaxy (low-velocity particles are captured more efficiently in the Sun, high-velocity particles leave clearer signals in direct detection experiments), as well as presenting different sensitivity to the structure of the dark matter halo (a local void or clump can deplete or enhance the possibilities for direct detection). IceCube has evaluated these data for evidence of dark matter annihilations in the Sun, in the Galactic Center, and in the Galactic Halo, searching for an excess neutrino flux over the expected atmospheric neutrino background, which provides the results of dark matter searches for WIMPs, Kaluza-Klein modes and super heavy candidates (Simpzillas), using the 79-string configurations of IceCube [63]. Given that the Sun is essentially a proton target and that the muon flux at the detector can be related to the capture rate of neutralinos in the Sun, the IceCube limits on the spin-dependent neutralino-proton cross section are currently well below the reach of direct search experiments, proving that neutrino telescopes are competitive in this respect. The simple assumption that dark matter is a thermal relic limits the maximum mass of the dark matter particle, which turns out to be a few hundred TeV for a thermal WIMP, the so called unitarity constraint. However, dark particles might have never experienced local chemical equilibrium during the evolution of the Universe, and their mass may be in the range much larger than the mass of thermal WIMPs, which have been called WIMPZILLAs [64, 65]. NTA can perform the most sensitive indirect search for WIMPZILLAs, with much better effective detection area for tau neutrinos from annihilation in the Sun, especially above  $\sim 10 \text{ PeV}$ , the complementary

sensitive energy region for IceCube.

Super-heavy particles ( $M \gtrsim 10^4$  GeV) produced during inflation may be the dark matter, independent of their interaction strength. Most popular ones are SIMPZILLAS, magnetic monopoles, supersymmetric Q-balls and nuclearites.

Strongly interacting super-heavy particles (SIMPZILLAs) will be captured by the Sun, and their annihilation in the center of the Sun will produce a flux of energetic tau neutrinos that should be detectable by neutrino telescopes [66].

Magnetic monopoles turn out to be consequence of most variants of Grand Unified Theories [67]. The electromagnetic energy losses of monopoles in the atmosphere, as well as neutrinos produced from monopole-antimonopole annihilations in the Sun and Earth, induce clear signatures in optical (Cherenkov and fluorescence) air-shower detectors like NTA [68].

Nuclearites (strange quark matter or strangelets) are hypothetical aggregates of u, d and s quarks, combined with electrons to adjust electric neutrality. Nuclearites, like meteors, produce visible light as they traverse the atmosphere. Their luminosity as a function of their mass is  $L=1.5\times 10^{-3}(M/1\mu\mathrm{g})$  watt [69]. For example, the apparent visual magnitude of a 20 g nuclearite at a height of 10 km is -1.4, equal to that of the brightest star, Sirius. Atmospheric nuclearites at galactic velocities ( $v\sim250\,\mathrm{km/s}$ ) can easily be distinguished from ordinary meteors bounded to the Solar System, moving no faster than 72 km/s. It could be identified with clear evidence with the wide FOV high resolution optical detector of NTA.

Q-balls are hypothetical coherent states of quarks, sleptons and Higgs fields [70]. Neutral Q-ball (Supersymmetric Electrically Neutral Solitons, SENS) could catalyse proton decay along their path, similar to GUT monopoles. Electrically charged Q-ball (Supersymmetric Electrically Charged Solitons, SECS) would produce light in a similar way as nuclearites.

# 2 Earth Skimming Tau Neutrino

### 2.1 Neutrino detection method

To detect VHE neutrinos, a large target volume is required in order to compensate for the very small neutrino-nucleus cross section. On that basis, the secondary particles produced by the first neutrino interaction must be detected in one way or another. The detection method using water and ice as a target detects Cherenkov light from secondary muons, taking advantage of the fact that ice and water are optically transmissive to some extent. This method can be categorized as the method in which the target and detection volumes are water and near-by rock surrounded by the water tank. On the other hand, the detection method using air-showers aims at the detection of higher-energy neutrinos. This method enables us to achieve a huge detection volume as the atmosphere has very high transmittance. However, it is difficult to obtain a larger target mass due to low atmospheric density. The detection method called Earth-skimming  $\nu_{\tau}$  technique [71, 72, 73, 74, 75] can realize a huge target mass and detection volume at the same time, by dividing the target and detection volume utilizing the interaction process of  $\nu_{\tau}$ . The detection method is described as follows (see Fig. 7). The VHE  $\nu_{\tau}$  interacts in the Earth or mountain and produces tau lepton  $(\tau)$ .  $\tau$  penetrates the Earth and/or mountain and appears in the atmosphere. Subsequently, it decays and produces an air-shower. Cherenkov photons from the air-shower are detected. Owing to the separation of the first interaction where  $\nu_{\tau}$  produces  $\tau$  and the  $\tau$  decay that generates the air-shower, air-shower observation becomes possible while preserving the huge

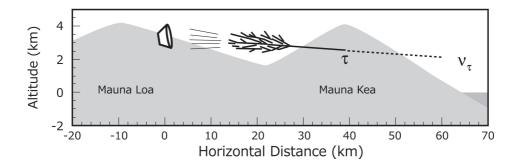


Figure 7: Schematic view of Cherenkov  $\tau$  shower ES method. Mauna Kea is used as the target mass for neutrino charged current interaction. The produced air-shower is observed from Mauna Loa. In addition to the fact that the mountain can be viewed with large solid angle from the observatory, the distance of about 30 km from the observatory to the Mauna Kea surface is appropriate for the air-shower development, resulting in the huge advantage of the Ashra-1 observatory.

target mass required for the first interaction. "Cherenkov  $\tau$  shower ES method" is defined as the detection method which detects Cherenkov photons from tau shower appearing from the Earth or the mountain fully utilizing this feature. We note, for example, that Mauna Kea is over 3,200 km<sup>3</sup> in volume and 9.3 tera tons in mass [76].

### 2.2 Deflection from parent tau neutrinos

This section describes deflection of Cherenkov  $\tau$  shower compared to the arrival direction of parent  $\nu_{\tau}$ , in order to estimate the ability to trace back to the accelerator based on the direction of the detected air-shower. We evaluate the deflection of the propagating particle in each step of neutrino charged current interaction,  $\tau$  propagation in the Earth, tau decay, and production of extensive air-shower. We use PYTHIA [77] to evaluate neutrino charged current interaction. Since  $P_{\tau} < M_W$  where  $P_{\tau}$  denotes the transverse momentum of a produced  $\tau$  and  $M_W$  denotes the mass of the W boson, the deflection angle  $\tau$  ( $\Delta\theta_{\tau}$ ) with respect to the parent  $\nu_{\tau}$  should be less than 0.3 arcmin for  $E_{\tau} > 1$  PeV. The simulation results with PYTHIA are consistent with this.

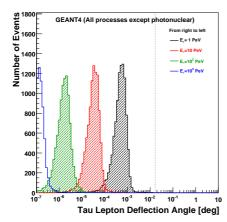
Second, we use GEANT4 [78] to evaluate the deflection of the  $\tau$  due to propagation in the Earth. To estimate the energy loss of high energy leptons, the following parametrization is generally adopted [79]:

$$-\left\langle \frac{dE}{dX}\right\rangle = \alpha + \beta E,$$

where  $\alpha$  denotes the nearly constant ionization loss, and  $\beta$  denotes the radiative energy loss due to Bremsstrahlung, pair production and photonuclear interaction. Since radiative energy loss is dominant for high energy  $\tau$ s, these high energy processes must be included in the "Physics List" of GEANT4. Thus, we apply the following processes originally defined for muons to  $\tau$ s, and estimated the deflection after propagating through 10 km of rock.

- G4MuBremsstrahlung: Bremsstrahlung
- G4MuPairProduction:  $e^+e^-$  pair production <sup>1</sup>
- G4MuNuclearInteraction: Photonuclear Interaction

<sup>&</sup>lt;sup>1</sup>We modified the original G4MuPairProduction so that momentum conservation includes the produced particles, resulting in the inclusion of deflection.



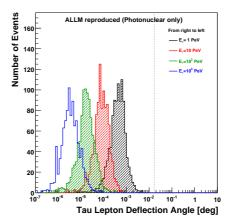


Figure 8: The simulation results of deflection angle of  $\tau$ s after propagating through 10 km of rock: (*Left*) the GEANT4 result including all high energy processes except for photonuclear interaction; (*Right*) the result of photonuclear interaction from custom simulation. Note that the decay of  $\tau$  was switched off for the above simulations. The hatched histograms indicate that the  $\tau$  range is less than 10 km.

To validate our GEANT4 simulation, we compare the energy dependence of  $\beta$  for Bremsstrahlung, pair production, and photonuclear interaction to Ref. [79]. The  $\beta$  energy dependence agrees well for the former two processes, but we find that GEANT4 produces smaller values for photonuclear interaction at higher energy, and that the difference is a factor of 3 at  $10^8$  GeV. We write accordingly a toy Monte Carlo simulation for photonuclear interaction using the formalism of Refs. [80, 81], reproducing the energy dependence of  $\beta$  within  $\pm 30$  % accuracy.

Fig. 8 shows the simulation results for  $\tau$  deflection after propagating through 10 km of rock. The left panel shows the GEANT4 result including all high energy processes except photonuclear interaction, while right panel shows our "homemade" simulation result for the latter. These results indicate that photonuclear interaction becomes dominant for deflection at 1 PeV and higher. Note that the decay of  $\tau$  was switched off for the above simulations, and the hatched histograms indicate that the  $\tau$  range is less than 10 km. For example, the  $\tau$  range is 4.9 km at 100 PeV. We conclude that the deflection angle of  $\tau$ s with energy greater than 1 PeV is much less than 1 arcmin.

Next, the deflection due to  $\tau$  decay is estimated by using the output of TAUOLA [82], taking into account  $\tau$  polarization. From the mass  $m_{\tau}$ , the deflection angle must be less than 1 arcmin if the energy of the secondary particle is higher than 13 TeV. Using TAUOLA output, it was shown that the probability to have deflection greater than 1 arcmin is quite small from the decay of PeV  $\tau$ s. We conclude that the deflection angle between decay particles which produce the air-shower and parent  $\nu_{\tau}$  is less than 1 arcmin.

Finally, we evaluate the direction of the hadron air-shower using CORSIKA. At the shower maximum, we compare the direction of the parent particle (charged pion) to that of electrons and positrons, the dominant producers of Cherenkov photons. We find that the angle between the average direction of electrons and positrons and parent particle of the air-shower is coincident within 0.1° at 1 PeV.

In conclusion, we find that the arrival direction of PeV  $\nu_{\tau}$ s is preserved within 0.1°, including the hadron air-shower generation. The accurate reconstruction of arrival direction by means of fine imaging will be a very powerful technique in the determination of the point sources of PeV  $\nu_{\tau}$ s.

### 3 The NTA Detector

The NTA observatory will consist of four sites, Site0, Site1, Site2, Site3, as shown in Fig. 3. The conceptual layout for the NTA observatory considers three site stations (Site1, Site2, and Site3) forming a 25 km-side triangle watching the total air mass surrounded by the mountains of Mauna Loa, Mauna Kea, and Hualalai. A single site station, Site0, at the center of the triangle has half-sky (extendable to full-sky) coverage. Each site has a centralized group of Detector Units (DU). One detector unit (Fig. 4) has a few Light Collecting systems (LC) with segmented mirrors. The features of the system were studied with the Ashra-1 station site constructed on Mauna Loa (3300 m a.s.l.).

In order to investigate the performance of the NTA detector, we shall use the following setup conditions of the assumed locations of observational sites of the NTA system on Hawaii Island.

- 1. The left side of Fig. 9 shows the layout of the NTA site locations. The local Cartesian coordinate system is defined with the origin at Site0, as denoted by "0" in Fig. 9, the positive z-axis points to the zenith, and the positive y-axis points north. The x-y coordinates of the site locations are from the projected x-y plane, with the z-coordinates from the corresponding height of the topography data of Hawaii Island.
- 2. The three observational sites, each located at the vertices of a triangle of equal 25 km side length, are: Site1 at Mauna Loa Ashra-1 location, Site2 on the slope of Mauna Kea, and Site3 on the slope of Hualalai.
- 3. The central observational site, Site0, is at the center of gravity of the above three site locations. Site1–Site3 are equidistant 14.4 km from Site0.
- 4. The location of Site1 and Site2 are set at the Ashra-1 Mauna Loa Observation Site (ML-OS), and at 25 km distant from ML-OS in the direction of Kilohana Girl Scout Camp, respectively.
- 5. After above settings, the locations of remaining two sites are automatically fixed.

The right part of Fig. 9 shows the layout of the four sites, superimposed on the topography map image of Hawaii, to be used as settings in the simulation program. Table 1 shows the x-y-z coordinates of the site locations and the detection FOV coverage, as determined from the above description. For the simulation study, given in the next section, we assume that each LC has the total FOV of  $32^{\circ} \times 32^{\circ}$ , trigger pixel FOV of  $0.5^{\circ} \times 0.5^{\circ}$ , and image sensor pixel FOV of  $0.125^{\circ} \times 0.125^{\circ}$ . The Site0 system consists of 12 LCs in the lower elevation angle regions, which together cover the half-sky solid angle that is  $\pi$  sr. The other sites have only 6 LCs in the lower elevation angle region, to cover the FOV of the half-sky solid angle which is  $\pi/2$  sr. The bottom edge of the lower elevation angle region is defined to be  $-9^{\circ}$  in elevation angle (  $9^{\circ}$  below the horizon ).

Fig. 10 shows the simulated panoramic views in altitude and azimuthal directions from the four NTA sites, with colours indicating the distance from the corresponding site.

### 4 The NTA Detector Performance

We investigate NTA performance with site location setup of previous Section.

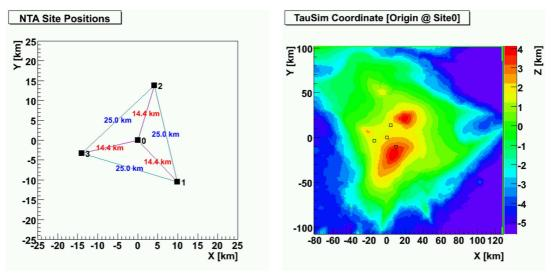


Figure 9: (left) The x-y coordinates of the four NTA site locations, with Site0 defined as the origin; (right) the Hawaii Island topography map superimposed with the four NTA site locations.

Site ID	Location	X [km]	Y [km]	Z [km]	FOV [sr]
Site0	Center	0.000	0.00	2.03	$\pi$
Site1	Mauna Loa	9.91	-10.47	3.29	$\pi/2$
Site2	Mauna Kea	4.12	13.82	1.70	$\pi/2$
Site3	Hualalai	-14.02	-3.35	1.54	$\pi/2$

Table 1: The x-y-z coordinates and detection FOV coverage of the four NTA sites, which are used in the simulation program. The location of Site0 is defined as the origin of the coordinate system.

#### 4.1 Propagation

For simulating the propagation of  $\nu_{\tau}$ s and  $\tau$ s in the Earth, we performed the following procedure and treatment.

- 1. The density profile of the Earth is chosen according to the Preliminary Earth Model [83, 84]. It depends strongly on the depth in the Earth as shown in Fig. 11. We modified the profile just for the density of the ground surface in the radius range of r > 6356 m from 2.6 g/cm<sup>3</sup> into 2.9 g/cm<sup>3</sup>, which is suitable for Basalt rock as the most common type of rock in the Earth's crust and most of the ocean floor around the Island of Hawaii.
- 2. We took into account both charged current interaction (CC) and neutral current interaction (NC) of  $\nu_{\tau}$ s and  $\tau$ s in the Earth. The energy dependence of the inelasticity parameter y for CC and NC based on the CTEQ4 parametrization are shown in [83], and no difference is seen between those for CC and NC.
- 3. We implement  $\nu_{\tau} \to \tau \to \nu_{\tau}$  regeneration in the simulation. Because of the short lifetime of the tau, regeneration can be an important effect as the  $\nu_{\tau}$  passes through a significant column depth through the Earth [79].
- 4. In simulating  $\tau$  propagation, the current position of  $\tau$  is evaluated at every step of the energy loss rate of 10%, unless the  $\tau$  comes out of the Earth or decays.

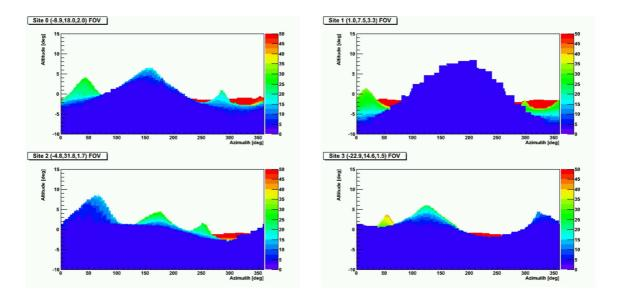


Figure 10: Panoramic views simulating the topographical image from NTA Site0 (top left), Site1(top right), Site2 (bottom left), Site3 (bottom right). Nearby obstacles with distance less than 3 km are neglected.

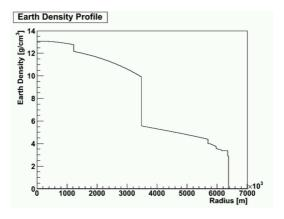


Figure 11: PREM (Preliminary Earth Model) density distribution of the Earth [83]

5. In the lab frame,  $\nu_{\tau}$  from  $\tau$  decay on average carries a fraction 0.4 of the  $\tau$  energy [85]. We used this constant average value of 0.4 as the energy of  $\nu_{\tau}$  from  $\tau$  decay, without taking into account the energy distribution. The error from this approximation can be neglected for the moment, because of the good agreement between results with our simulation and with ANIS (All Neutrino Interaction Simulation) [86], as shown in Fig. 12.

Fig. 12 shows the distribution in the plane of  $E_{\tau}$  and dip angle (minus elevation angle;  $-\theta_{elev}$ ) in the case of primary  $\nu_{\tau}$  energy of  $10^{18}$  eV.

The left side shows the case of neglecting any effect from  $\nu_{\tau} \to \tau \to \nu_{\tau}$  regeneration or NC interaction of  $\nu_{\tau}$  in the Earth, while the right side shows the case of taking into account both effects from  $\nu_{\tau} \to \tau \to \nu_{\tau}$  regeneration and NC interaction of  $\nu_{\tau}$  in the Earth. Each bin content in these figures is given by:

$$\frac{d^2 N_{\tau}}{dE_{\tau} d\Omega} (E_{\tau}, \theta) \times d \log_{10} E_{\tau} \cdot 2\pi d\theta.$$

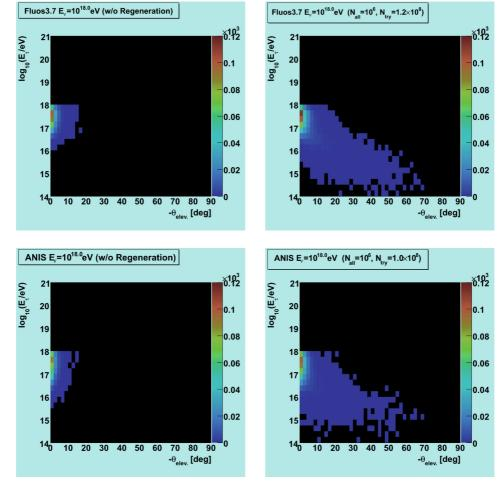


Figure 12: Distribution in the  $E_{\tau}$  and dip angle (minus elevation angle;  $-\theta_{elev}$ ) plane in the case of primary  $\nu_{\tau}$  energy of  $10^{18}$  eV.

Fig. 12 (bottom) shows the result using ANIS [86], which is approved for use for AMANDA and IceCube, and acknowledged well for detailed interactions, decays, and propagation of  $\nu_{\tau}$ s and  $\tau$ s. In general, the results with our simulation and ANIS agrees reasonably well. From detailed comparison, we should consider systematic errors of ~12% on produced  $\tau$  flux in the Earth in using our simulation program.

#### 4.2 Simulation

Before evaluation of the performance of NTA using our simulation program, we summarize our settings at the following three steps.

- 1. Simulation for the Earth-skimming  $\nu_{\tau} \to \tau$ 
  - $\nu_{\tau}$  (CTEQ4) [87]
  - Inelasticity parameter [83]
  - Energy loss in the Earth [88, 79]
- 2. Air-shower simulation:  $\tau \to \text{Cherenkov}$  and fluorescence light
  - τ Decay (approximated; [89])
  - Air-shower generation (Gaisser-Hillas + NKG) [89]

$\nu_{\tau}$ Energy	• • • •	$L_{\rm CC}$	$\theta_{ m elev}^{ m c}$
$10^{15} {\rm \ eV}$	$6.342 \times 10^{-34} \text{ cm}^2$	$2.62 \times 10^9 \text{ g/cm}^2$	$-30.6^{\circ}$
$10^{16} {\rm \ eV}$	$1.749 \times 10^{-33} \text{ cm}^2$	$9.49 \times 10^8 \text{ g/cm}^2$	$-13.0^{\circ}$
$10^{17} \text{ eV}$	$4.436 \times 10^{-33} \text{ cm}^2$	$3.74 \times 10^8 \text{ g/cm}^2$	$-5.71^{\circ}$
$10^{18}~{ m eV}$	$1.049 \times 10^{-32} \text{ cm}^2$	$1.58 \times 10^8 \text{ g/cm}^2$	$-2.45^{\circ}$
$10^{19} \text{ eV}$	$2.379 \times 10^{-32} \text{ cm}^2$	$6.98 \times 10^7 \text{ g/cm}^2$	$-1.08^{\circ}$

Table 2: Based on CTEQ4 [87], differential  $\nu_{\tau}$  CC cross section ( $\sigma_{\rm CC}$ ), corresponding interaction length ( $L_{\rm CC}$ ), and the critical angle ( $\theta_{\rm elev}^c$ ) such that the chord thickness at the critical angle corresponds to  $L_{\rm CC}$ . For the Earth density profile, we refer to the parametrization of PREM [86, 83].

#### 3. Detector simulation:

- light collection and throughput of light
- simplified triggering logic
- Event reconstruction is not implemented yet.

We assume the following input parameters.

Light Collection Area:  $A = 7.07 \text{ m}^2$  (equivalent with the effective pupil diameter of  $\phi 3 \text{ m}$ )

Optical filter transmittance:  $\epsilon_{\rm filt} = 90\%$ 

Quantum efficiency of photoelectric tube:  $\epsilon_{\rm QE}=24\%$ 

LC FOV:  $32^{\circ} \times 32^{\circ}$ 

Trigger pixel FOV:  $0.5^{\circ} \times 0.5^{\circ}$  / trigger pixel

Exposure time in trigger pixel:  $t_{trigpix} = 50$  ns

Required trigger condition:

To estimate the detection sensitivity of NTA the event candidates must satisfy the following requirements:

• total number of photoelectrons detected in one LC must satisfy:

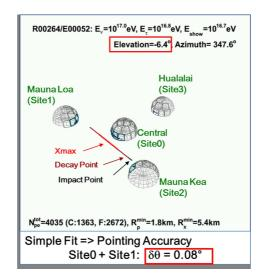
$$N_{\mathrm{pe}}^{\mathrm{LC}} > 61,$$

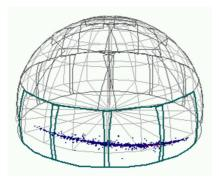
• S/N estimated in the track-associated box of the width of 4 pixels and the length of 64 pixels, which includes the candidate event air-shower track, must satisfy:

$$S/N > 4$$
,

where the standard deviation of night sky background in the track-associated box with the exposure of 50 ns is estimated as  $\sigma(N_{\rm pe}^{\rm BG})=15.4$  pe from a night sky background estimate [90] given by  $2.0\times10^5{\rm photons/m^2/sr/\mu s}$ .

A simulated Earth-skimming  $\tau$  shower event with primary  $\nu_{\tau}$  energy of  $E_{\nu} = 10^{17} \text{eV}$  using the above settings is shown in Fig. 13. The reconstructed air-shower axis with simple fits to the Cherenkov and fluorescence hit map images taken by the two sites reproduces the primary  $\nu_{\tau}$  arrival direction with an error of 0.08°.





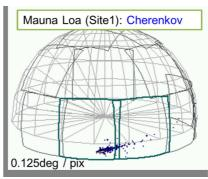


Figure 13: A simulated Earth-skimming  $\tau$  shower event with primary  $E_{\nu\tau} = 10^{17}$  eV, which has both fluorescence image taken by Site0 and Cherenkov by Site1. (top) Global hit map view in the NTA system; (bottom left) air-shower fluorescence image taken by Site0, and (bottom right) Cherenkov image from the same event taken by Site1. The trigger pixel and fine image FOVs are  $0.5^{\circ} \times 0.5^{\circ}$  and  $0.125^{\circ} \times 0.125^{\circ}$ , respectively.

### 4.3 Sensitivity

We estimate the effective detection area for  $\nu_{\tau}$  fluence from a point source with our simulation program for Earth-skimming  $\tau$  showers incorporating the appropriate Earth model [84], the topography around the NTA observatory, the interaction and propagation process of  $\nu_{\tau}$  and  $\tau$  in the Earth [83, 86], the decay of  $\tau$  and generation of air-shower, with parameter choices as described before.

We define the critical dip angle (minus critical elevation angle;  $-\theta_{elev}^c$ ) as the chord thickness at the dip angle  $-\theta_{elev}^c$  that corresponds to the CC interaction length  $L_{\rm CC}(E_{\nu})$ , determined by the interaction cross-section  $\sigma_{\rm CC}(E_{\rm CC})$  for a  $\nu_{\tau}$  traveling with energy  $E_{\nu}$ . Table 2 shows differential cross sections of  $\nu_{\tau}$  CC interaction  $\sigma_{\rm CC}$  based on CTEQ4 [87], the corresponding interaction length  $L_{\rm CC}$ , and  $\theta_{\rm elev}^c$  for each  $E_{\nu_{\tau}}$  between 1 PeV and 10 EeV.

Taking into account the critical dip angles for the energies of  $\nu_{\tau}$  in Table 2, we estimated the effective detection areas for  $\nu_{\tau}$  from a point source with azimuthal arrival direction corresponding to that of the Mauna Loa summit  $(\phi_2)$  and that of the Hualalai summit  $(\phi_3)$ , with respect to the central site of Site0, and dip angles of  $2.0^{\circ}$ ,  $-2.0^{\circ}$ ,  $-5.0^{\circ}$ ,  $-10.0^{\circ}$ ,  $-20.0^{\circ}$ , and  $-30.0^{\circ}$ , as shown in Fig. 15.

Fig. 16 shows the differential sensitivities, as a function of  $E_{\nu_{\tau}}$  for a point source of  $\nu_{\tau}$ ,

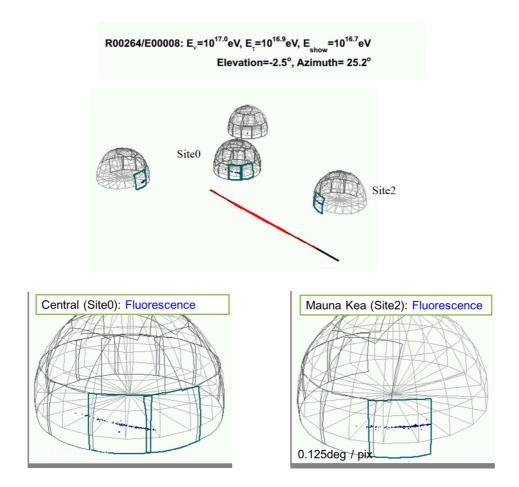


Figure 14: Similar with 13 but in the case of the detection of stereoscopic fluorescence signals.

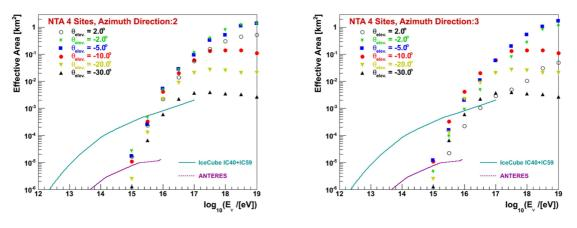
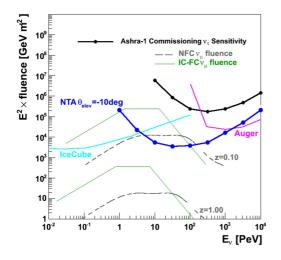


Figure 15: Estimated effective detection area simulated for  $\nu_{\tau}$  from a point source with azimuthal arrival direction corresponding to (left) Mauna Loa ( $\phi_2$ ) and (right) Hualalai ( $\phi_3$ ) with respect to the central site of Site0, and dip angles of 2.0° (black open circle),  $-2.0^{\circ}$  (green star),  $-5.0^{\circ}$  (blue filled box),  $-10.0^{\circ}$  (red filled circle),  $-20.0^{\circ}$  (yellow filled triangle), and  $-30.0^{\circ}$  (black filled triangle).



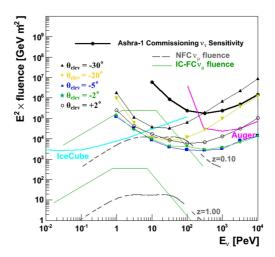


Figure 16: Comparison of differential sensitivities as function of  $E_{\nu_{\tau}}$  for a point source of  $\nu_{\tau}$ , calculated as the Feldman-Cousins 90% CL limit event number for null expected events, using a light collector (LC) from Ashra-1 commissioning [10] and the NTA layout of LCs, in the cases of (left)  $\theta_{\rm elev} = -10^{\circ}$ , (right)  $\theta_{\rm elev} = +2^{\circ}$  (opencircle),  $-2^{\circ}$  (green),  $-5^{\circ}$  (blue),  $-20^{\circ}$  (yellow), and  $-30^{\circ}$  (black). The sensitivities published from IceCube [91] and Pierre Auger Observatory [92] are shown, as well as theoretical estimates used for the former (solid lines) and recalculated by Hümmer et al. (dashed lines) [93] assuming the distance of  $z \sim 0.1$  and 1.0.

calculated as in [94] requiring 2.3 events in a bin size of one energy decade  $\Delta \ln E_{\nu}$ . The 2.3 events is the Feldman-Cousins 90% CL limit event number for null expected events.

Fig. 17 (top) shows the diffuse sensitivities for  $\nu_{\tau}$  fluxes with NTA for 3 year observation time. Both differential and integral sensitivities are given. The sensitivity limit is defined as  $2.3E_{\nu}/(S\Omega_{\rm eff}\cdot\Delta T)$ . Also shown is the comparison between NTA, Pierre Auger Observatory [92] and IceCube [95], various model predictions for cosmogenic  $\nu$ s, as well as other experiments of RICE, AMANDA, and ANITA are superimposed [96]. For the diffuse sensitivities of NTA, we assume the duty of 10% for 3 years observation ( $\sim 9.5 \times 10^6$  s) and trigger conditions as described before.

### 4.4 Exposure

From Fig. 15, NTA can survey  $\nu_{\tau}$  point sources with best sensitivity in detection solid angle for  $\nu_{\tau}$  defined as  $-30^{\circ} < \theta_{\text{elev}} < 0^{\circ} \times 0^{\circ} < \phi_{\text{azi}} < 360^{\circ}$  in the primary  $\nu_{\tau}$  energy region of 10 PeV  $< E_{\nu_{\tau}} < 1$  EeV. From Fig. 16, the survey depth can be better than redshift z < 0.1 corresponding to a distance of  $\sim 400$  Mpc.

With the observational conditions assumed as follows:

• Solar elevation angle:  $< -18^{\circ}$ 

• Lunar bright surface ratio: < 0.2

• Ideal weather efficiency: 100%

the total duty is estimated to be 20.5%, which corresponds to maximum observation time of 1800 hours per year.

Fig. 18 shows the exposure map for the observation with NTA on Hawaii Island (the Site1 position: 19°32′28″ N, 155°34′03″ W, 3294 m a.s.l.), with Mollweide projection in Galactic

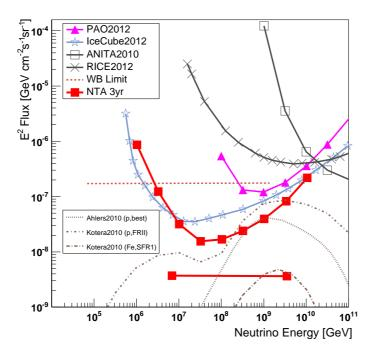


Figure 17: Diffuse sensitivities for  $\nu_{\tau}$  fluxes with NTA for 3 years observation time. Both differential sensitivity (curve) and integral sensitivity assuming the E<sup>-2</sup> flux spectrum (horizontal line) are shown. The sensitivity limit is defined as  $2.3E_{\nu}/(S\Omega_{\rm eff}\cdot\Delta T)$ . Comparison among NTA, Pierre Auger Observatory [92] and IceCube [95], same as the top one but various model predictions for cosmogenic  $\nu$ s, as well as other experiments of RICE, AMANDA, and ANITA are superimposed [96]. For NTA, the duty of 10% for 3 year observation ( $\sim 9.5 \times 10^6$  s) is assumed.

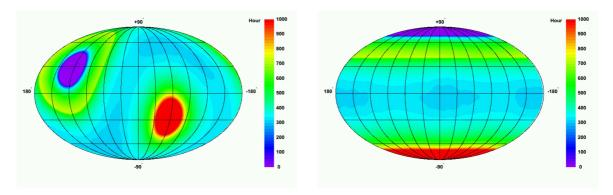


Figure 18: Exposure map for observation with NTA on Hawaii Island (the Site1 position:  $19^{\circ}32'28''$  N,  $155^{\circ}34'03''$  W, 3294 m a.s.l.), with Mollweide projection in Galactic (left) and Equatorial (right) coordinates. Maximum observation time is normalized to 1000 hours per year (red), where NTA can detect with maximum efficiency (total duty of 11.4%).

(left) and Equatorial (right) coordinates on the celestial sphere. The maximum observation time is normalized to 1000 hours per year, as shown in red in the figure where NTA can detect with maximum efficiency, which means total duty of 11.4%, corresponding to about half the above ideal case. The location of NTA on Hawaii Island allows us to enjoy a survey of our galactic center for more than several hundred hours each year.

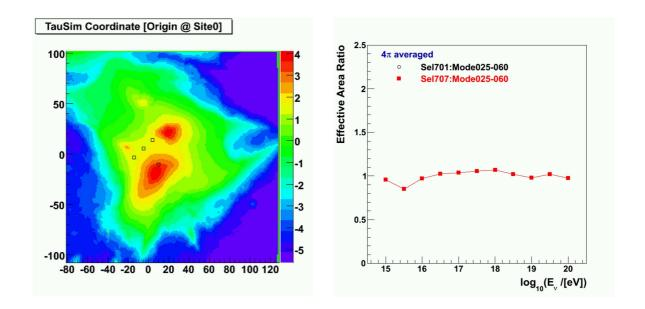


Figure 19: (left) Modified layout of NTA sites, and (right) ratio of the two sets of effective detection area for  $\nu_{\tau}$ s as a function of  $E_{\nu_{\tau}}$ , obtained with modified and regular layouts (Fig. 9). The location of Site0 is changed into the midpoint between Site2 and Site3.

### 4.5 Effect of Changing Site Layout

To check the effect of changing the site layout on the detection sensitivity of NTA, we changed only the location of Site0 into the midpoint between Site2 and Site3, as shown in Fig. 19 (left), and repeated the sequence of simulation for diffuse sources as before. The right side of Fig. 19 shows the ratio of the two sets of effective detection area for  $\nu_{\tau}$ s as a function of  $E_{\nu_{\tau}}$ , which are obtained with modified layout and regular one. We do not see any significant change over all energies in the PeV-EeV region. The layout can therefore be adapted to practical concerns.

### 4.6 Angular resolution

As discussed in Section 2.2, a Cherenkov  $\tau$  shower with E > 1 PeV preserves the arrival direction of the parent  $\nu_{\tau}$  to within 0.1° accuracy. This means that the ability of the detector to reconstruct the arrival direction results in the precise identification of the VHE neutrino sources and leads to the realization of "multi-particle astronomy". Owing to its high-resolution imaging capability, the NTA detector has a huge potential to improve the reconstruction of the arrival direction of  $\nu_{\tau}$ -induced air-showers.

NTA will observe quasi-horizontal air-showers with the primary energies between PeV and EeV. Note that the location of the shower maximum in the atmosphere, i.e., the depth of maximum development  $X_{\rm max}$  is expected to be roughly in the range of 500-1000 g/cm<sup>2</sup> from the first interaction in the atmosphere for tau decays of different energies [97][98]. The depth range corresponds to the length of 6-12 km along the air-shower axis assuming the averaged atmospheric pressure of 0.7 atm. The shower axis is defined as the extension of the initial momentum vector of the incident tau decay particle in the direction of cascade propagation. The particle density in the shower core, i.e., in the central region, is very high and drops rapidly with increasing the core distance from the shower axis. Electron lateral distribution functions (LDFs) of air-showers are well described by Nichimura-Kamata-Greisen (NKG) functions [99][100]. The LDFs measured by KASCADE in the energy range

from  $5\times10^{14}$  eV up to  $10^{17}$  eV can be reproduced accurately for the fit parameter of electron lateral distributions  $r_{\rm e}\sim20\text{-}30$  m with fixing  $s\sim1.6\text{-}1.8$ , which are different from the original Molière radius  $r_{\rm M}$  and age parameter s in the NKG functions [101]; the latter are used in the Monte Carlo simulation here. In addition, Monte Carlo simulations of air-showers find steeper LDFs than the NKG distribution in higher energies [98].

Let us first we try a back-of-envelope estimate, for example, an image of 1000 photoelectrons detected by a light collector, which originated from an air-shower trajectory with the Gaussian LDF of  $\sigma=30$  m the track length of 6 km as a typical event. From the image, we can determine the shower detector plane (SDP) with accuracy of  $\sim 0.2$  mrad (0.6 arcmin) purely in a statistical way, neglecting the error due to image resolution, although real LDF around the air-shower axis is exponential and steeper than the Gaussian distribution. This means air-shower developments are fairly useful for pointing back to the original source, and detector resolution dominantly limits the determination of arrival direction of air-showers. Ashra-1 has already achieved a few arcmin imaging resolution including optical alignment errors, and NTA will be operated with the resolution  $\sim 1.5$  mrad (5 arcmin). In that case, the SDP direction will be determined with the accuracy of 15 m, which is finer than the measured shower LDF parameter of  $r_{\rm e}$ , at the distance of 10 km as a typical case.

The simulated air-shower event shown in Fig. 14 provides a more concrete and realistic example. The  $\nu_{\tau}$  is generated at the energy of 100 PeV with the elevation angle of -2.5°, which is a quasi-horizontally upward event. The converted  $\tau$  emerges from the earth with energy 73 PeV and decays into particles which induce an air-shower of 46 PeV. The fluorescence light generated from the air-shower is triggered by light collectors deployed at Site0 and Site2. The closest approaches or the impact parameters ( $R_{\rm P}$ 's) to the air-shower axis are 9.8 km and 12 km from the Site0 and Site2 respectively, and the distances to the  $X_{\rm max}$  from Site0 and Site2 are 16 km and 12 km respectively. Due to the design of the layout of the four sites, i.e. the 25 km-side triangle (Site1,2,3) with the centered site (Site0) as shown in Fig. 3, almost all air-shower axes which pass the air volume above the inner triangle area of NTA have the closest approach of less than 12.5 km to one of the four sites. Therefore, the simulated event shown in Fig. 14 is an example with relatively poor signal of all generated events of the same primary energies.

Fig. 20 shows photo-electron images (red cross marks) on the plane of the altitude and azimuthal angles, which are triggered and taken from the same event shown in Fig. 14 by light collectors at Site0 and Site2. The SDPs that correspond to the true air-shower axis (light green dotted line) and tilted by  $\pm 0.2^{\circ}$  (light green solid line) are indicated on the same figure. Note that the LDFs used in this analysis is the traditional NKG functions with the fixed Molière radius  $r_{\rm M}=79$  m and a variable age parameter s in the NKG form, not the steeper LDF recently measured by KASCADE. Even with the traditional NKG form the dominant components of photo-electrons of the image is between the boundaries of the SDPs tilted by  $\pm 0.2^{\circ}$  with respect to that of the true air-shower axis. For the simple fit adopted here, to eliminate the statistical fluctuation in the altitude angle coordinate, profile histograms are used to display and fit the mean values of altitude angles in rebinned azimuthal bins, which are also shown in Fig. 20. The mean values based on the profile histograms reproduce the locations of true air-shower axis well. The image and trigger pixel resolutions assumed here are 0.125° and 0.5° respectively. With the combined images taken at Site0 and Site2, the SDP can be reproduced with fit error of 0.02°. Note that we can further improve the reconstruction accuracy here especiallyly in the higher energies by using more sophisticated likelihood fit analysis and expected shower developments for each shower energy with the advantage of high resolution images, beyond our present simple treatment of profiling the lateral distribution on the alt-azimuth coordinate plane. In the literature [102], we have described the detailed Monte Carlo study of the angular resolution only

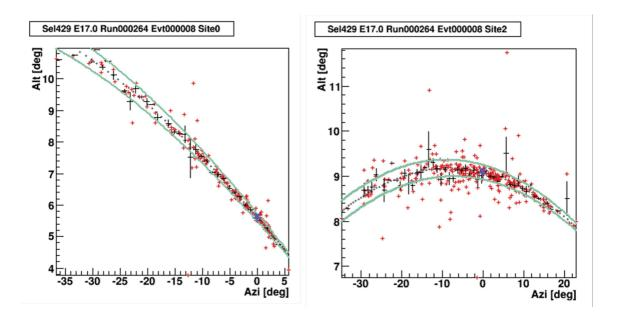


Figure 20: Simulated photo-electron images of air-shower development (red cross marks) in the alt-azimuth coordinates of light collectors installed at Site0 and Site2. The shower detector plane (SDP) with the true air-shower axis (light green dotted line) and those tilted by  $\pm 0.2^{\circ}$  with respect to the SDP based on the true air-shower axis of which primary energy is  $10^{17}$  eV and altitude angle is  $-2.5^{\circ}$ .

for monostatic observation of Cherenkov images of  $\tau$  showers generated by earth-skimming PeV-EeV  $\nu_{\tau}$  events with the Ashra-1 detector system. In that work, we confirm that a likelihood analysis with fine images of shower core structures compared with Monte Carlo expectation of air-shower development improves significantly the arrival direction resolution. The sophisticated and completed likelihood analysis using Monte Carlo simulated air-shower developments is beyond the scope of this LoI, before determining detailed detector design but with only assumed baseline concepts.

For pointing back to  $\nu_{\tau}$  sources, we simultaneously fit observed data with the four parameters of  $(\phi_{SDP}, \theta_{SDP})$  of the normal unit vector of SDP and the impact parameter  $R_{\rm P}$  and the arrival direction angle  $\chi_0$  of the air-shower axis constrained on the SDP of the event. The detailed definitions of  $\chi_0$  and  $R_P$  on SDP can be seen in the Fly's Eye detector paper [103]. In the case of reconstruction of quasi-horizontal air-showers, however, purely geometrical bistatic method is not useful, since the opening angles between two of SDPs observed with light collectors at different sites are nearly flat, i.e. 180° and strongly correlated with each other. For the determination of  $\nu_{\tau}$  source positions, particularly for  $\chi_0$  and  $R_{\rm P}$  on SDP, we should fully utilize the timing information recorded by the trigger pixel sensor in the NTA system as well as the image data. Our realistic baseline design of the trigger pixel sensor system has its pixel FOV of  $0.5^{\circ} \times 0.5^{\circ}$  and the least time stamp resolution of each trigger pixel of 10 ns. An advantage of the baseline trigger design based on the developments of Ashra-1 is that we can optimize pixel and timing resolutions of imaging system and trigger systems independently. For each event, after determining these four parameters, they are transformed into another set of parameters, i.e. the arrival direction of the air-shower axis  $(\phi_{AS}, \theta_{AS})$  and the position  $(X_{\tau}, Y_{\tau}, Z_{\tau}(X_{\tau}, Y_{\tau}))$  where the  $\tau$  emerges from the mountain. The Z coordinate of the emerging point  $Z_{\tau}(X_{\tau}, Y_{\tau})$  is obtained from a topographic map as a function of X and Y coordinates. For the aim of partially demonstrating the performance of simultaneous fit of parameters needed to point back to sources of observed  $\nu_{\tau}$  candidates,

we have prepared for Monte Carlo data simulating  $\nu_{\tau}$  events with the energies of every half decade between  $10^{15.5}$  eV and  $10^{19}$  eV with fixed altitude angle of  $-2.0^{\circ}$  and fixed azimuthal angle toward the peak of Mauna Kea.

Fig. 21 shows the results of fitting Monte Carlo data. The blue filled square marks with error bars show the total RMS resolution of the reconstructed  $\tau$  arrival direction as function of logarithmic energies of generated  $\nu_{\tau}$ s. The red filled triangle marks with error bars show the total RMS resolution of the polar angle component of the reconstructed  $\tau$  arrival direction as function of logarithmic energies of generated  $\nu_{\tau}$ s, which is important to eliminate cosmic ray background events due to misreconstruction of the arrival directions as described in the next subsection. Fig. 21 also shows the event rate of multistatic observation, that is ratio of events observed with DUs at two or more sites, which is another result from this Monte Carlo simulation study. Although the accuracy of the angular resolution increases, the multistatic rate is seen saturated above  $10^{17}$  eV, which indicates the limitation of this simple fit method using profiling LDS at each bin of longitudinal development along the air-shower axis.

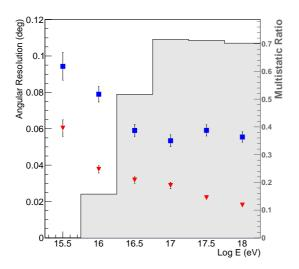
This simple method works well when the core structure is negligible. Although the NTA detectors with high resolution imagers resolve out the shower core structures for high energy events, we treated the shower axis as a line without any lateral structure. At higher energies, the effect of the shower core structure become significant. Again likelihood analysis with fitting functions made of enough number of Monte Carlo events taking into account the shower lateral and longitudinal development more consistently, the resolution should be recovered particularly in the higher energy region. Even using the simple fit method for quasi-horizontal  $\tau$  shower events with Monte Carlo events with the altitude angle of  $-0.2^{\circ}$ , we have confirmed the pointing resolution of  $0.1^{\circ}$ - $0.06^{\circ}$ . For the altitude angle or inclination of SDP, they can be determined within an error of 0.06- $0.02^{\circ}$ . Detailed and precise Monte Carlo studies of the NTA detector system will be performed elsewhere, at step of the detector design report, after the publication of this LoI.

For the moment, we quote the estimate of the angular resolution to be less than  $0.2^{\circ}$  as a fairly conservative estimate from simulated events of monostatic Cherenkov images in the most pessimistic case of reconstruction of images taken with the NTA detector system.

### 4.7 Background

In this subsection, we evaluate the background events due to air-showers. Background events due to the detector itself are discussed in Ref. [10]. Air-shower background candidates are normal cosmic rays, muons, muon neutrinos,  $\tau$ s, and  $\nu_{\tau}$ s. From simple flux calculations, it is shown that the neutrino components through mountain, prompt  $\tau$  components and muons are negligible [104, 105, 106, 107, 108]. Thus, we consider normal cosmic rays with large zenith angles, of which arrival directions are misreconstructed, as the dominant background contamination in this study. To evaluate the rate of the background contamination due to the directional misreconstruction, we count the air-shower events which pass through the sky region above mountain edges or horizon within assumed gap angles. To simulate normal cosmic ray air-showers we use CORSIKA in the same way as with the  $\nu_{\tau}$  simulation with a thinning parameter of  $10^{-5}$  as a result of confirming it to be acceptable. Assuming the maximum weather efficiency of 100%, 1750 hr of observation time on Hawaii Island is expected in one year. We use the trigger pixel threshold of 20 photoelectrons as a realistic sensitivity which is same as the Ashra-1 DU one. The results are shown in Table 3.

From this Monte Carlo study, we estimate the background contamination rate for the observation of NTA. We require that the arrival direction of the candidate event must emerge from earth or mountain. Background events may pass through the requirement of the direction of air-shower axis direction due to the misreconstruction of air-shower events. However, the background rate should be very low and almost free. From the geography of Hawaii Is-



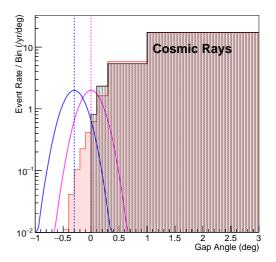


Figure 21: Angular resolutions of reconstructed arrival directions of  $\tau$  from Mauna Kea. The RMS resolutions of the reconstructed  $\tau$  arrival direction (blue filled square marks with errors) and the polar angle components (red filled square marks with errors) improves with energy. Multistatic rate (shaded histogram), i.e. ratio of events observed from two or more sites saturates above  $10^{17}$  eV.

Figure 22: Estimate for cosmic ray background contaminations due to misreconstruction of their arrival directions. True angle with respect of the mountain edge (Hatched histogram) and observed angles (red filled histogram) assuming the angular resolution of  $0.2^{\circ}$  after smering out the true angular distribution. Two probability density functions for signal  $\tau$ s with the arrival directions of  $0.0^{\circ}$  and  $-0.3^{\circ}$ . The integrated areas of these histograms are normalized to be the expected event rate/year/DU.

Gap angle $\delta\theta$ (°)	0.1	0.3	1.0	3.0
CR rate (showers/yr/DU)	0.082	0.55	4.3	39

Table 3: The annual rate of cosmic ray showers which pass through the sky regions within assumed gap angles and detected with NTA with the trigger pixel threshold of 20 photoelectrons.

land and the layout of the NTA sites, this directional misreconstruction is potentially caused only near the edge between earth/mountain and atmosphere. We make Monte Carlo estimates for ordinary cosmic ray air-showers of which axis pass through the gap spaces of the solid angle just above mountain edge as described above.

For this aim, we make a histogram of differential event rate evaluated from the result listed in Table 3 and smear out the distribution by the angular resolution to quantitatively estimated the leakage into our  $\tau$  shower candidate sample from the outside of the fiducial volume of NTA. Fig. 22 shows the differential distribution of true air-shower axis directions for ordinary cosmic rays (black shaded histogram) and the expected observed air-shower directions after smearing them by very conservative angular resolution of  $0.2^{\circ}$  (red pearskin finish), which is derived after detailed Monte Carlo studies on the directional reconstruction for Cherenkov air-showers in comparison of the reconstruction with fluorescence light

detection as shown in the previous section.

As a result, the rates of cosmic rays which pass over the mountain edge (0° in Fig. 22) and constrained boundary of solid angle below the mountain edge by  $0.3^{\circ}$  are estimated to be 0.08 events/year and 0.006 events/year for one DU with the FOV of  $32^{\circ} \times 32^{\circ}$ . Fig. 22 also shows the probability density function for one event just on the edge (pink curve) and that on the fiducial limit  $0.3^{\circ}$  below the mountain edge, where all histograms are normalized for the integrated area to be annual event rate for each DU respectively.

In the case of the fiducial solid angle restricted after cutting  $< 0.3^{\circ}$  with respect to the mountain edge, total CR contamination rate in the NTA detector system with 30 DUs is estimated to be  $\sim 0.2/\text{yr}$  and the efficiency of the effective aperture for Earth-skimming  $\nu_{\tau}$ s to be  $\sim 90$  %. We can realize the almost background-free condition without sacrificing the superior sensitivity of NTA for detecting Earth-skimming  $\nu_{\tau}$ s using good advantages of high resolution images and the pointing accuracy.

## 5 Time Frame, Organization, and Funding

At the present time, we are investigating various options for the site, organization, and the design of instruments. Also, we intend to invite other groups to either contribute directly to this project, or to join us on the site with their complementary instruments. The resulting synergy effects would benefit all parties, avoid unnecessary parallel technical developments, and lead to cost savings for the different projects. It is clear that collaboration forming is key to success of the NTA scientific goal. The time frame for the proposed project is thus given both by considerations of budgetary and scientific aspects. In March 19–20, 2014, a preliminary workshop (VHEPA2014) was held at Kashiwa campus of the University of Tokyo to discuss the design of the project and plans with interested colleagues. In April 8-9, 2015 a small workshop, successive to VHEPA2014, was held at National Taiwan University to discuss the scientific goals and promotion of the project. We plan to have an informal meeting to discuss post-IceCube project new detector project at the 34th International Cosmic Ray Conference (ICRC) held from July 30 to August 6, 2015, in The Hague.

In January, 2016 we plan to hold a workshop as VHEPA2016 at University of Hawaii Manoa to discuss more detailed physics and NTA potential performance, funding processes, and make ready for a white paper of the project as basic documents to use for the funding requests in each country.

We have already set up the International Executive Board (IEB) of NTA for decision making and steering the collaboration since October 12, 2012. Some IEB members have already submitted funding requests to exchange information, detector design, meetings, and construction of the detector. IEB selects the representative who becomes the spokesperson of the collaboration. Each country has a Local Institutional Board (LIB), which is composed of representatives from institutes in the country. LIB selects the representative who becomes a member of IEB. We will set up various Working Groups (WGs) as real working bodies. WG leaders are nominated by LIB and decided by IEB.

Major decisions concerning the hardware implementation should be undertaken in 2015, toward the publication of Project Proposal. In the subsequent two years, components should be developed and tested, and we should continue to request the Japanese government for construction funding. We can eliminate critical developments by using experience from Ashra-1 and NuTel projects. We aim at installing the first detector site and starting commissioning operation in early 2017, if we succeed in the primary Japanese funding in time. We plan to start the operation using at least a part of Site0 and Site1 of proposed four sites by 2018, with the primary construction budget covering at least 1/4 of full operation cost. Once we succeed in the primary funding request and start construction of the first sites, we start the

request for matching funds to the governments of various collaborating countries. We aim at starting construction of Site2 and Site3 with the matching funds from countries other than Japan.

Since major choices concerning implementation details are still open at this time, it does not seem appropriate to discuss a detailed cost breakdown. To provide a guideline, however, we have estimated in some detail the cost of one design variant, with major components of the detector either covered by offers from potential manufacturers (light collector mount, mirrors, trigger-readout sensors and electronics, and so on), or extrapolating from well-known costs of the Ashra-1 instruments. On this basis, we estimate the production cost per light collector in the 20M yen range, plus total R&D costs of about 100M to 150M yen. One detector unit (DU), as shown in Fig. 1, requires four light collectors and one trigger and readout unit, so the rough cost estimate is 100M yen per DU. We plan to build at least 12, 6, 6, and 6 DUs at Site0, Site1, Site2, and Site3, respectively, for the coverage of FOV as shown in Table 1, assuming the FOV for DU to be  $32^{\circ} \times 32^{\circ}$ . 30 DUs are needed for covering the total FOV. We do not include infrastructure costs such as site access, site preparation, light collector shelters, networking, and so on. Roughly speaking, at least 100M yen per DU is needed from the experience of construction of Ashra-1 at Mauna Loa. The current crude estimate is 5000M yen for the construction of NTA.

The Ashra-1 collaboration has agreed to continue the observation at the Mauna Loa site as well as explore the NTA system, at least by the time NTA starts the construction. In order to explore the hardware and software components, the Ashra-1 experience is recognized as an important and useful demonstration of the challenging new detection techniques.

## Acknowledgment

We thank P. Binder and J. Goldman from University of Hawaii Hilo for their useful comments and help. Many thanks to the Ashra-1 and NuTel collaborations for their cooperation. The Ashra Experiment is supported by the Coordination Fund for Promoting Science and Technology and by a Grant-in-Aid for Scientific Research from the Ministry of Education, Culture, Sports, Science and Technology of Japan.

### References

- [1] A. Loeb and E. Waxman. Journal of Cosmology and Astroparticle Physics, 2006(05):003, 2006.
- [2] M. G. Aartsen et al. Phys. Rev. Lett., 111:021103, 2013.
- [3] IceCube Collaboration et al. Science, 342(6161):1242856, 2013.
- [4] M G Aartsen, R Abbasi, M Ackermann, and J Adams. Probing the origin of cosmic rays with extremely high energy neutrinos using the IceCube Observatory. *Physical Review D*, 2013.
- [5] J. Abraham et al. Phys. Rev. Lett., 104:091101, 2010.
- [6] M. Sasaki. J. Phys. Soc. Jpn., 77SB:83, 2008.
- [7] M. Sasaki. Proc. of ICRR2000 Satellite Symposium: Workshop of Comprehensive Study of the High Energy Universe, pages 109–124, 2000.
- [8] S. Barwick. *Physica Scripta.*, T85:106, 2000.

- [9] Y. Asaoka and M. Sasaki. Nucl. Instrum. Methods Phys. Res. A, 647:34, 2011.
- [10] Y. Aita et al. The Astrophysical Journal Letters, 736(1):L12, 2011.
- [11] Y. Aita et al. GCN Circular, 8632, 2008.
- [12] Y. Asaoka et al. GCN Circular, 11291, 2010.
- [13] George WS Hou and MA Huang. arXiv preprint astro-ph/0204145, 2002.
- [14] M. Sasaki, A. Kusaka, and Y. Asaoka. Nuclear Instruments and Methods in Physics Research A, 492:49–56, 2002.
- [15] M. Sasaki, Y. Asaoka, and M. Jobashi. Nuclear Instruments and Methods in Physics Research A, 501:359–366, 2003.
- [16] J. K. Becker. Physics Reports, 2008.
- [17] K. Murase, M. Ahlers, and B. C. Lacki. Phys. Rev. D, 88:121301, 2013.
- [18] P. Baerwald, M. Bustamante, and W. Winter. *The Astrophysical Journal*, 768(2):186, 2013.
- [19] V. S. Berezinsky and G. T. Zatsepin. *Physics Letter B*, 28:423, 1969.
- [20] V. Ptuskin, V. Zirakashvili, and E.-S. Seo. The Astrophysical Journal, 718(1):31, 2010.
- [21] A. Calvez, A. Kusenko, and S. Nagataki. Phys. Rev. Lett., 105:091101, 2010.
- [22] K. Kotera and A. V. Olinto. Astronomy and Astrophysics, 2011.
- [23] R. Aloisio, V. Berezinsky, and A. Gazizov. *Journal of Physics: Conference Series*, 2012.
- [24] G. Giacinti, M. Kachelrieß, D. V. Semikoz, and G. Sigl. *Journal of Cosmology and Astroparticle Physics*, 2012(07), 2012.
- [25] N. Gupta. Astroparticle Physics, 48(0):75 77, 2013.
- [26] N. Gupta. Astroparticle Physics, 2011.
- [27] L. A. Anchordoqui et al. Journal of High Energy Astrophysics, 1:1–30, 2014.
- [28] A. M. Hillas. Journal of Physics G: Nuclear and Particle Physics, 31(5):R95, 2005.
- [29] A. Dar and R. Plaga. A&A, 349:259–266, 1999.
- [30] J. Hinton. New Journal of Physics, 11(5):055005, 2009.
- [31] A. Kappes et al. The Astrophysical Journal, 656(2):870, 2007.
- [32] F. A. Aharonian et al. Nature, 432:75-77, 2004.
- [33] F. Aharonian et al. A&A, 437:L7–L10, 2005.
- [34] F Aharonian et al. Nature, 439(7077):695–698, 2006.
- [35] M. Ahlers and K. Murase. Physical Review D, 2014.
- [36] F. Aharonian et al. Astronomy & Astrophysics, 425(1):L13–L17, 2004.

- [37] F. Aharonian et al. A&A, 448:L43–L47, 2006.
- [38] M. Hoshino, J. Arons, Y. A. Gallant, and A. B. Langdon. ApJ, 390:454–479, 1992.
- [39] D. Horns et al. A&A, 451:L51–L54, 2006.
- [40] B. Link and F. Burgio. Monthly Notices of the Royal Astronomical Society, 371(1):375–379, 2006.
- [41] A. Bhadra and R. K. Dey. Monthly Notices of the Royal Astronomical Society, 395(3):1371–1375, 2009.
- [42] F.A. Aharonian et al. J. Phys. Conf. Ser., 39:408, 2007.
- [43] I. F. Mirabel. Science, 312:1759, 2006.
- [44] A. A. Abdo et al. The Astrophysical Journal, 688(2):1078, 2008.
- [45] L. A. Anchordoqui et al. ArXiv e-prints, 2013.
- [46] M. Su, T. R. Slatyer, and D. P. Finkbeiner. *The Astrophysical Journal*, 724(2):1044, 2010.
- [47] S. Razzaque. Phys. Rev. D, 88:081302, 2013.
- [48] P. Mészaros. Rep. Prog. Phys., 69:2259, 2006. and references therein.
- [49] M. Ackermann et al. ApJ, 716(2):1178, 2010.
- [50] J. A. Nousek et al. ApJ, 642(1):389, 2006.
- [51] D. Burlon et al. The Astrophysical Journal Letters, 685:L19, 2008.
- [52] K. Murase et al. The Astrophysical Journal Letters, 651:L5, 2006.
- [53] T. Kifune G. Sinnis F.A. Aharonian, J. Buckley. Rep. Progr. Phys., 71:096901, 2008.
- [54] W. Benbow et al. Proc. 30th Int. Cosmic Ray Conf., Merida, Mexico, 3:1081, 2007.
- [55] H. Krawczynski et al. Astrophys. J., 601:151, 2004.
- [56] F. Acero and others (H.E.E.S. Collaboration). Science, 326:1080, 2009.
- [57] N. Karlsson et al. arXiv preprint arXiv:0912.3807, 2009.
- [58] K. Greisen. Phys. Rev. Lett., 16:748–750, 1966.
- [59] G.T. Zatsepin and V.A. Kuz'min. JETP Lett. (USSR) (Engl. Transl.), 4, 1966.
- [60] M. Ahlers et al. Astroparticle Physics, 34(2):106–115, 2010.
- [61] M. Ave et al. Astroparticle Physics, 23(1):19–29, 2005.
- [62] R.C. Cotta, J.S. Gainer, J.L. Hewett, and T.G. Rizzo. New Journal of Physics, 11(10):105026, 2009.
- [63] M. G. Aartsen et al. Phys. Rev. Lett., 110:131302, 2013.
- [64] D.J. Chung, E.W. Kolb, and A. Riotto. *Physical Review D*, 59(2):023501, 1998.

- [65] P. Blasi, R. Dick, and E.W. Kolb. Astroparticle Physics, 18(1):57 66, 2002.
- [66] I.F.M. Albuquerque, L. Hui, and E.W. Kolb. Phys. Rev. D, 64:083504, 2001.
- [67] G. Giacomelli, S. Manzoor, E. Medinaceli, and L. Patrizii. *Journal of Physics: Conference Series*, 116(1):012005, 2008.
- [68] S.D. Wick, T.W. Kephart, T.J. Weiler, and P.L. Biermann. Astroparticle Physics, 18(6):663 687, 2003.
- [69] A. De Raújula and S.L. Glashow. Nature, 312(5996):734–737, 1984.
- [70] A. Kusenko. *Physics Letters B*, 405(1-2):108 113, 1997.
- [71] G. Domokos and S. Kovesi-Domokos. 433:390, 1998.
- [72] A. Letessier-Selvon. AIP Conf. Proc., 566:157, 2000.
- [73] E. Zas H. Athar, G. Parente. Physical Review D, 62:093010, 2000.
- [74] D. Fargion. ApJ, 570:909, 2002.
- [75] F. Wilczek T. Yu J. Feng, P. Fisher. Phys. Rev. Lett., 88:161102, 2002.
- [76] E. Wolfe, W. Wise, and G. Dalrymple. U.S. Geological Survey Professional Paper, 1557:129, 1997.
- [77] T. Sjöstrand et al. Comput. Phys. Commun., 135:238, 2001.
- [78] S. Agostinelli et al. Nucl. Instrum. Methods A, 506:250, 2003.
- [79] S. Iyer Dutta et al. *Physical Review D*, 63:094020, 2001.
- [80] H. Abramowicz and A. Levy. arXiv:hep-ph/9712415v2, 1997.
- [81] B. Badelek and J. Kwiecinski. Rev. Mod. Phys., 68:445, 1996.
- [82] S. Jadach et al. Comput. Phys. Commun., 76:361, 1993.
- [83] R. Gandhi et al. Astropart. Phys., 5:81, 1996.
- [84] A. M. Dziewonski and D. L. Anderson. *Physics of the Earth and Planetary Interiors*, 25:297, 1981.
- [85] J. F. Beacom, P. Crotty, and E. W. Kolb. Phys. Rev. D, 66:021302, 2002.
- [86] A. Gazizov and M. Kowalski. Computer physics communications, 172(3):203–213, 2005.
- [87] R. Gandhi et al. *Physical Review D*, 58:093009, 1998.
- [88] J. Tseng et al. *Physical Review D*, 68:063003, 2003.
- [89] M. Sasaki, Y. Asaoka, and M. Jobashi. Astropart. Phys., 19:37, 2003.
- [90] M. Sasaki. J. Phys. Soc. Jpn., 70(Suppl. B):129, 2001.
- [91] R. Abbasi et al. Nature, 484(Supplemental information):351, 2012.
- [92] J. Abraham et al. *Physical Review D*, 79:102001, 2009.

- [93] S. Hümmer, P. Baerwald, and W. Winter. Phys. Rev. Lett., 108:231101, 2012.
- [94] G. J. Feldman and R. D. Cousins. *Physical Review D*, 57(7):3873, 1998.
- [95] R. Abbasi et al. Phys. Rev. D, 83:092003, 2011.
- [96] T.K. Gaisser. High energy neutrinos from space. arXiv preprint arXiv:1201.6651, 2012.
- [97] PKF Grieder. Average Development and Properties of the Hadronic Moonic and Electromagnetic Components in Showers of 10\*\*4 to 10\*\*7 GEV Derived from AN All.... International Cosmic Ray Conference, 1979.
- [98] A M Hillas and J Lapikens. Electron-photon cascades in the atmosphere and in detectors. *International Cosmic Ray Conference*, 1977.
- [99] K Greisen. Cosmic Ray Showers. Annual Review of Nuclear and Particle Science, 10:63–108, 1960.
- [100] K Kamata and J Nishimura. The Lateral and the Angular Structure Functions of Electron Showers. *Progress of Theoretical Physics Supplement*, 6:93–155, 1958.
- [101] T Antoni et al. Electron, muon, and hadron lateral distributions measured in air showers by the KASCADE experiment. *Astroparticle Physics*, 14(4), 2001.
- [102] Y. Asaoka and M. Sasaki. Astroparticle Physics, 41:7–16, 2013.
- [103] R. M. Baltrusaitis et al. Nucl. Instrum. Methods A, 240:410, 1985.
- [104] Y. Aita et al. 31th Intl. Cosmic Ray Conf. (Lodz), ID0313, 2009.
- [105] E. Zas et al. Astropart. Phys., 1:297, 1993.
- [106] R. Enberg et al. Physical Review D, 78:043005, 2008.
- [107] A. D. Martin et al. Acta Physica B, 34:3273, 2003.
- [108] H. Athar et al. Astropart. Phys., 18:581, 2003.